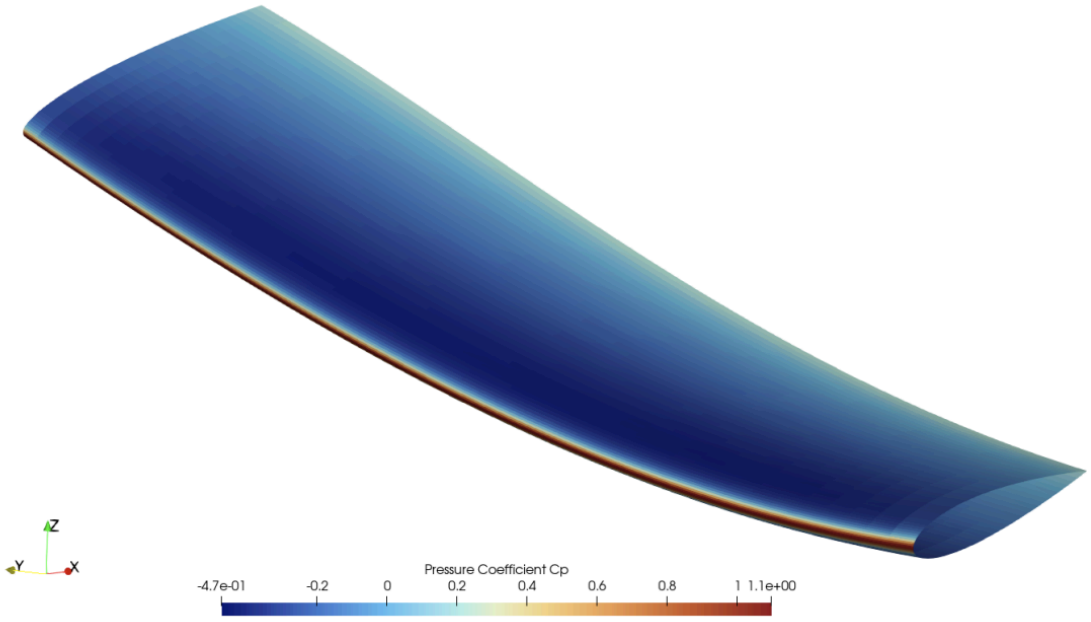
Gecko

Design for IGA-type discretization workflows

Gecko Technical Report 3

DC04 - Juan Ignacio Camarotti



This project has received funding from the European Union's Horizon Europe research and innovation programme under grant agreement No 101073106
Call: HORIZON-MSCA-2021-DN-01

Funded by the European Union

Deliverable Information sheet

Version	Date	Author	Document history/approvals
0		Marco Zuñiga	Draft version circulated to partners
1	24.10.2026	Juan I. Camarotti	Adding information
2	26.10.2026	Ricky Aristio	Revising
3	26.10.2026	Juan I. Camarotti	Final document

Executive summary

This technical report summarizes the research activities carried out in 2026 within the framework of the GECKO Project, focusing on the development of consistent interface mapping strategies and partitioned co-simulation methodologies for multiphysics problems involving Isogeometric B-Rep Analysis (IBRA). The overarching objective is to facilitate the integration of high-fidelity isogeometric structural models with independently discretized fluid and acoustic solvers, ensuring accurate and consistent information transfer across non-matching interfaces while preserving the flexibility of partitioned solution approaches.

Building upon the developments of previous years, which established the foundations for interface mapping and demonstrated coupled aeroelastic and vibroacoustic workflows, the research activities in 2026 concentrated on three complementary directions: the coupling of IBRA and conventional Finite Element Method (FEM) discretizations, the development of geometrically nonlinear beam-to-surface mapping strategies for fluid–structure interaction (FSI), and the further investigation of partitioned vibroacoustic co-simulation using isogeometric structural and acoustic formulations. Particular attention was devoted to the kinematic consistency of interface transfers, the conservation of virtual work, and the numerical robustness of coupling algorithms.

The first research direction addressed interface mapping between IBRA and conventional FEM discretizations. The coexistence of spline-based and standard finite element representations introduces challenges associated with non-matching interface geometries, different approximation spaces, and the transfer of kinematic and mechanical quantities. The work investigated strategies for exchanging displacements and forces between independently discretized structural interfaces, with emphasis on maintaining consistency and enabling the integration of CAD-based structural models into existing multiphysics simulation environments.

The second research direction focused on the coupling of geometrically nonlinear isogeometric beam models with fluid interfaces. Since beam formulations describe structural deformation through centerline displacements and rotational degrees of freedom, their integration into surface-based FSI frameworks requires a suitable reconstruction of the surrounding fluid interface. The work considered both Euler–Bernoulli and Timoshenko beam formulations, addressing the transfer of structural kinematics to the fluid boundary and the corresponding mapping of distributed fluid loads to generalized beam forces and moments. The developed framework was assessed through analytical deformation cases and representative FSI benchmarks, with particular attention to large rotations, mapping accuracy, and the consistency of the exchanged interface quantities.

The third research direction investigated partitioned vibroacoustic co-simulation in the frequency domain, combining isogeometric structural analysis with Boundary Element Method (BEM) formulations for exterior acoustics. This approach enables the treatment of structural vibration and acoustic radiation using specialized solvers while avoiding the volumetric discretization of the surrounding unbounded acoustic domain. The study examined the coupling of structural and acoustic subproblems through non-matching interfaces, including the treatment of complex-valued interface quantities and the convergence behavior of partitioned coupling algorithms. Numerical investigations involving representative structural configurations were

used to assess the accuracy of the coupled response and the robustness of the solution procedure.

Overall, the research activities presented in this report contribute to the development of a flexible computational framework for multiphysics simulations involving isogeometric structural discretizations. By addressing interface mapping at different levels of structural representation, from multipatch IBRA surfaces to geometrically nonlinear beams, and extending partitioned coupling strategies to frequency-domain vibroacoustics, the work advances the integration of CAD-based analysis models into modular co-simulation environments. These developments provide a foundation for future applications to increasingly complex aeroelastic, fluid–structure interaction, and vibroacoustic problems.

Table of contents

Deliverable Information sheet 2
Executive summary 3
Table of contents 5
List of figures 6
List of abbreviations 7
Introduction 8
1. Monolithic vs Partitioned Approaches in Multiphysics Simulations 10
2. Isogeometric Analysis 11
    2.1 Isogeometric B-Rep Analysis (IBRA) 12
3. Governing Equations and Partitioned Coupling 14
    3.1 Fluid–Structure Interaction 14
    3.2 Interface Data Transfer 15
    3.3 Partitioned Solution Procedure 15
    3.4 Frequency-Domain Vibroacoustic Coupling 15
4. Interface Mapping 17
    4.1 Interface Representation and Transfer Requirements 17
    4.2 Mapping Strategies 18
        4.2.1 Nearest-Neighbor Mapping 18
        4.2.2 Nearest-Element Mapping 18
        4.2.3 Radial Basis Function Mapping 19
        4.2.4 Mortar Mapping 19
    4.3 Numerical Assessment: Three-Dimensional Lid-Driven Cavity 20
        4.3.1 Midpoint Displacement and Coupling Iterations 21
        4.3.2 Spatial Convergence of the Mapping Error 22
        4.3.3 Computational Cost 23
    4.4 Discussion 24
5. Consistent Beam Mapping for Fluid–Structure Interaction 26
    5.1 Beam Kinematics and Interface Reconstruction 26
    5.2 Consistent Transfer of Interface Loads 27
    5.3 Numerical Assessment: Mok FSI Benchmark 28
        5.3.1 Configuration and Coupling Interface 28
        5.3.2 Coupled Response 29
    5.4 Discussion 30
6. Partitioned Co-simulation for CAD-integrated Vibroacoustic Analysis 31
    6.1 Coupling Architecture and Interface Transfer 31
    6.2 Complex-Valued Convergence Acceleration 32
    6.3 Numerical Example: Spherical Shell in an Acoustic Fluid 32
    6.4 Discussion 35
7. Conclusions 36
8. References 37

List of figures

Figura 1: System matrix level of the monolithic approach 10
Figura 2: System matrix level of the partitioned approach 10
Figura 3: Representation of a trimmed NURBS surface 12
Figura 4: Nearest-neighbor mapping between non-matching IBRA–IBRA and IBRA–FEM interfaces 18
Figura 5: Nearest-element mapping between non-matching IBRA–IBRA and IBRA–FEM interfaces 19
Figura 6: Construction of the common integration domain for the IBRA–FEM mortar mapper 20
Figura 7: Three-dimensional lid-driven cavity benchmark: boundary conditions and fluid discretization 21
Figura 8: Midpoint displacement and coupling iterations for different interface mapping strategies 22
Figura 9: Spatial convergence of the mapping error for the smooth displacement field at t = 10 s 23
Figura 10: Spatial convergence of the mapping error for the displacement field at t = 2 s 23
Figura 11: Computational cost of mapping operator construction and application 24
Figura 12: Reference attachment of a fluid-interface point to the isogeometric beam centerline 27
Figura 13: Geometry and boundary conditions of the Mok FSI benchmark 28
Figura 14: Non-matching beam–fluid interface and displacement and force transfer directions 29
Figura 15: Fluid velocity magnitude and deformed interface in the Mok benchmark at t = 8 s and t = 20 s 29
Figura 16: Horizontal tip displacement and pressure histories for the Mok FSI benchmark 30
Figura 17: Data exchange architecture in partitioned vibroacoustic co-simulation 31
Figura 18: Spherical-shell vibroacoustic benchmark configuration and boundary conditions 33
Figura 19: Independent structural and acoustic multipatch discretizations of the spherical shell 34
Figura 20: Acoustic pressure magnitude for undamped and Rayleigh-damped spherical-shell configurations 34
Figura 21: Acoustic pressure phase angle for the Rayleigh-damped spherical shell 34
Figura 22: Acoustic pressure error and coupling convergence behavior using complex IQN-ILS 35

List of abbreviations

CAD	*Computer-aided Design*
FEM	*Finite Element Method*
FSI	*Fluid-Structure Interaction*
IBRA	*Isogeometric B-Rep Analysis*
RBF	*Radial Basis Functions*
SPL	*Sound Pressure Level*
IQN-ILS	*Interface Quasi-Newton with Inverse Least-Squares.*
ALE	*Arbitrary Lagrangian Eulerian*
BEM	*Boundary Element Method*
RBF	*Radial Basis Function*

Introduction

Numerical simulation plays a central role in the analysis and design of aerospace and mechanical engineering systems, particularly for lightweight structures subjected to complex loading conditions. In many applications, the structural response is influenced by interactions with surrounding physical fields, including aerodynamic forces, fluid pressure, and acoustic waves. Accurately capturing these interactions requires computational approaches capable of combining different physical models while maintaining numerical accuracy, stability, and computational efficiency.

In practical engineering applications, the individual physical domains are often represented using different numerical formulations and discretization techniques. Structural mechanics may be described using the Finite Element Method (FEM) or Isogeometric Analysis (IGA), whereas fluid dynamics and acoustics may rely on finite volume, finite element, or boundary element formulations. The integration of these methods becomes particularly relevant when different levels of model fidelity are required within the same simulation. For instance, reduced-dimensional structural models can provide an efficient representation of slender components, while higher-fidelity surface models may be necessary to capture local deformation or complex structural behavior. Combining such representations requires suitable strategies for exchanging information between independently discretized computational domains.

Partitioned co-simulation provides a flexible framework for addressing these multiphysics problems by allowing each physical subproblem to be solved independently using a dedicated numerical solver. In contrast to monolithic approaches, which assemble the coupled governing equations into a unified system, partitioned methods preserve the existing numerical formulations and software implementations of the participating solvers. This modularity facilitates the integration of specialized computational tools and the combination of different discretization techniques. However, the accuracy and robustness of partitioned simulations depend strongly on the treatment of the coupling interfaces. In particular, non-matching discretizations require appropriate mapping operators to transfer displacements, rotations, forces, and other interface quantities while preserving the relevant kinematic and mechanical properties. Furthermore, strongly coupled problems may require iterative coupling algorithms to ensure convergence and stability.

These challenges become particularly relevant when incorporating isogeometric structural models into partitioned simulation environments. IGA employs spline-based basis functions to represent both the computational geometry and the solution fields, offering improved geometric accuracy and higher-order continuity compared with conventional finite element discretizations. Isogeometric B-Rep Analysis (IBRA) extends this concept to complex CAD boundary representations, including trimmed and multipatch geometries. Within Kratos Multiphysics, IBRA provides a framework for the structural analysis of such geometries using formulations including Kirchhoff–Love shells. Nevertheless, coupling these models with conventional discretizations introduces additional requirements for interface mapping, particularly when the participating models differ in their geometric representation, approximation spaces, or available degrees of freedom.

An additional challenge arises when coupling reduced-dimensional structural formulations with fluid models defined on two- or three-dimensional interfaces. Beam formulations, for example, describe structural deformation through centerline kinematics, whereas fluid solvers typically require displacements and forces distributed over the surrounding wetted surface. Establishing a consistent connection between these representations requires reconstructing the fluid interface from the structural degrees of freedom and transferring the resulting fluid loads back to the beam. For geometrically nonlinear problems, this transfer must account for finite rotations

and the associated changes in cross-sectional orientation. The consistency of the displacement and force mappings is particularly important to preserve the mechanical work exchanged between the coupled domains.

Beyond time-domain fluid–structure interaction, partitioned coupling also presents specific challenges in frequency-domain vibroacoustics. In these problems, structural vibrations generate acoustic pressure fields, which may in turn influence the structural response through acoustic loading. The Boundary Element Method (BEM) is particularly suitable for exterior acoustic problems because it accounts for the radiation condition at infinity without requiring a volumetric discretization of the surrounding unbounded domain. Coupling BEM with isogeometric structural formulations provides an attractive approach for predicting sound radiation from CAD-based structural models. However, the exchange of complex-valued interface quantities, the treatment of non-matching discretizations, and the convergence of iterative coupling algorithms require particular consideration.

Building upon the developments reported in previous years, the research activities presented in this report focus on advancing interface mapping methodologies and partitioned co-simulation strategies involving isogeometric structural models. The work is organized around three main research directions. The first investigates the coupling of IBRA and conventional FEM discretizations, addressing the consistent transfer of interface quantities between different structural representations. The second develops geometrically nonlinear beam-to-surface mapping strategies for Euler–Bernoulli and Timoshenko beam formulations, enabling their integration into surface-based fluid–structure interaction simulations. The third examines partitioned vibroacoustic co-simulation using isogeometric structural and boundary element acoustic formulations, with emphasis on interface treatment and the convergence of coupling algorithms.

Together, these developments contribute to the integration of isogeometric and reduced-dimensional structural models into flexible multiphysics simulation environments. The objective is to establish consistent and robust coupling methodologies that facilitate the reuse of specialized solvers and support the analysis of increasingly complex fluid–structure interaction and vibroacoustic problems.

1. Monolithic vs Partitioned Approaches in Multiphysics Simulations

In multiphysics problem-solving, two primary approaches are widely used: monolithic and partitioned strategies.

Monolithic Approach
The monolithic approach involves solving all governing equations simultaneously within a unified framework. This method leads to a more stable and robust formulation, as all physical interactions are accounted for within a single system of equations.

However, the monolithic strategy often results in a large, complex global system that can be difficult to solve, especially as the size of the problem increases. As the global system grows, the conditioning of the system tends to worsen, making it more computationally demanding. Despite these challenges, the monolithic approach offers high accuracy and robustness, making it well-suited for certain complex multiphysics problems.

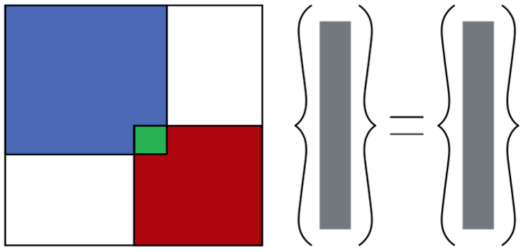


Figure 1: *System Matrix Level of the Monolithic Approach*

Partitioned Approach
In contrast, the partitioned approach separates the problem into distinct subsystems, solving each independently while coupling them through data exchange, often in the form of boundary conditions.

This approach allows for the reuse of existing single-field solvers, a key advantage in the co-simulation philosophy, where different physical domains are solved independently. The partitioned method is modular, flexible, and scalable, enabling the integration of different solvers for various disciplines. However, it is often less robust than the monolithic approach, as the coupling between subsystems may introduce stability challenges, particularly in highly coupled or stiff problems.

Despite this, partitioned approaches are more flexible and allow for easier integration of specialized solvers, making them valuable for complex multidisciplinary simulations.

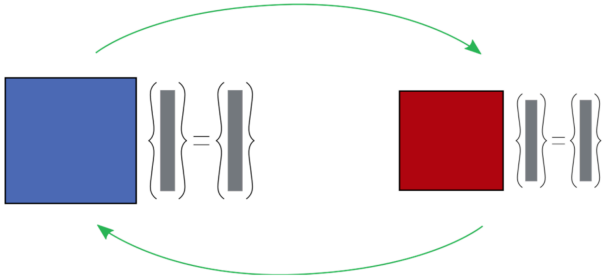


Figure 2: *System Matrix Level of the Partitioned Approach*

2. Isogeometric Analysis

Isogeometric Analysis (IGA), introduced by Hughes et al. [1], establishes a direct connection between Computer-Aided Design (CAD) and numerical analysis by employing the same spline-based functions for the representation of the computational geometry and the approximation of the solution fields. In contrast to conventional finite-element discretizations, where the geometry is typically approximated using element-based interpolation functions, IGA retains the spline representation employed in CAD. This provides an accurate description of curved geometries and enables higher-order continuity across element boundaries.

The most commonly employed basis functions in IGA are B-splines and Non-Uniform Rational B-Splines (NURBS). A univariate B-spline basis is defined by its polynomial degree p and a non-decreasing knot vector

$$\Xi = \{\xi_1, \xi_2, \ldots, \xi_{n+p+1}\}.$$

The basis functions are constructed recursively using the Cox–de Boor formula. For $p = 0$, the functions are piecewise constant, while higher-degree basis functions are obtained through

$$N_{i,p}(\xi) = \frac{\xi - \xi_i}{\xi_{i+p} - \xi_i} N_{i,p-1}(\xi) + \frac{\xi_{i+p+1} - \xi}{\xi_{i+p+1} - \xi_{i+1}} N_{i+1,p-1}(\xi),$$

where terms with zero denominators are defined as zero.
NURBS basis functions are obtained by introducing positive weights w_i into the B-spline representation:

$$R_{i,p}(\xi) = \frac{N_{i,p}(\xi) w_i}{\sum_{j=1}^{n} N_{j,p}(\xi) w_j}.$$

For surface geometries, tensor products of univariate basis functions are employed. The corresponding NURBS surface is expressed as

$$S(\xi, \eta) = \sum_{i=1}^{n} \sum_{j=1}^{m} R_{ij}^{p,q}(\xi, \eta) P_{ij},$$

where P_{ij} are the control points and $R_{ij}^{p,q}$ are the bivariate rational basis functions of polynomial degrees p and q.

The same basis functions are employed to approximate the unknown solution fields. For example, the structural displacement field can be written as

$$u^h(\xi, \eta) = \sum_{i=1}^{n} \sum_{j=1}^{m} R_{ij}^{p,q}(\xi, \eta) u_{ij},$$

where u_{ij} denote the displacement coefficients associated with the control points. Unlike conventional Lagrange finite elements, the control points generally do not lie on the physical geometry. Consequently, the solution coefficients do not necessarily correspond to physical nodal values, and field quantities must be evaluated through the spline basis.

An important characteristic of spline-based discretizations is their controllable continuity. For a B-spline basis of degree p, an interior knot of multiplicity r provides C^{p-r} continuity. Thus, maximum continuity of C^{p-1} can be achieved at simple interior knots. This property is particularly advantageous for structural formulations involving higher-order derivatives, such as Kirchhoff–Love shells and geometrically nonlinear Bernoulli beams.

In the context of partitioned multiphysics simulations, the spline-based representation also influences the treatment of coupling interfaces. Since the physical interface is not generally defined by a set of interpolatory nodes, transferring quantities between IGA and conventional discretizations requires mapping procedures that account for the geometry and approximation properties of the participating interfaces.

2.1. Isogeometric B-Rep Analysis (IBRA)

Although conventional IGA provides a direct connection between CAD geometry and numerical analysis, its application to complex engineering geometries presents additional challenges. CAD models are commonly constructed from multiple NURBS patches and may include trimming curves, which define the active regions of the underlying parametric surfaces. Such geometric representations cannot always be analyzed directly using standard tensor-product IGA discretizations.

Isogeometric B-Rep Analysis (IBRA) extends the isogeometric concept to CAD boundary representations, allowing trimmed and multipatch spline geometries to be incorporated into numerical analysis. In this approach, the original CAD surfaces provide the geometric representation, while the computational domain is defined by the active regions bounded by the corresponding trimming curves.

For a trimmed surface, the physical geometry can be described through the mapping

$$x = S(\xi, \eta), \qquad (\xi, \eta) \in \Omega_{trim},$$

where Ω_{trim} denotes the active region of the parametric domain. Since trimming curves may intersect the underlying knot spans, numerical integration must account for partially active elements. This requires suitable integration procedures that respect the trimmed geometry.

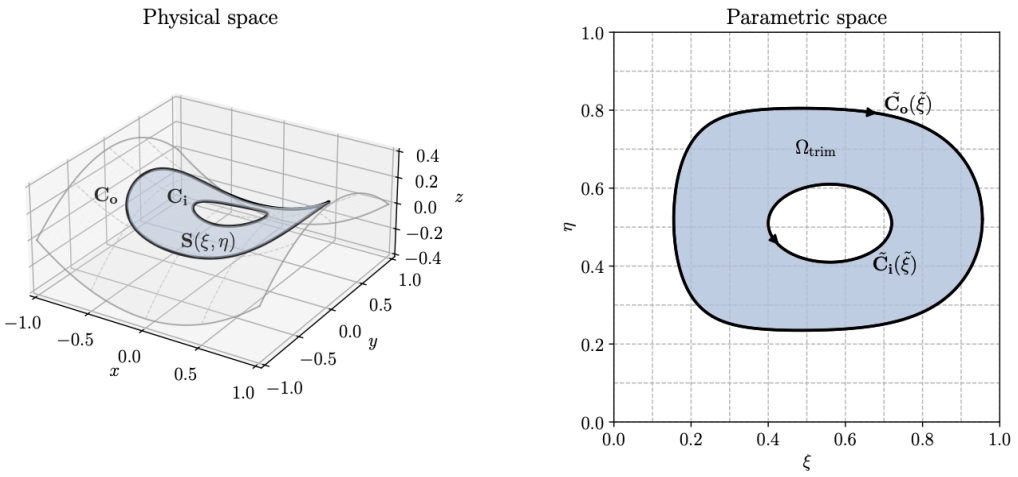


Figure 3: *Representation of a trimmed NURBS surface*

Complex structures may also consist of multiple independently parameterized spline patches. Although the patches can describe a geometrically continuous surface, their approximation spaces are generally independent. Consequently, continuity across patch interfaces must be addressed through appropriate numerical treatments when required by the structural formulation.

These characteristics make IBRA particularly suitable for structural analyses involving CAD-derived shell geometries, including trimmed and multipatch configurations. At the same time, they introduce specific challenges in partitioned multiphysics simulations. The coupling interface may consist of several independently parameterized patches, and the exchanged quantities must be transferred between spline-based fields and conventional finite-element or finite-volume representations.

The distinction becomes especially relevant when evaluating interface mapping algorithms. Accurate transfer requires consideration of the physical surface geometry, the parametric representation, and the approximation spaces of the participating discretizations. These aspects form the basis of the interface mapping developments presented in the subsequent section.

3. Governing Equations and Partitioned Coupling

The three research activities considered in this report share a partitioned computational setting, but they differ in their governing equations and in the quantities exchanged at the coupling interface. The interface conditions must therefore be distinguished from the numerical procedures used to transfer them between non-matching discretizations. This section introduces the common mechanical setting for fluid–structure interaction (FSI) and outlines the corresponding frequency-domain coupling conditions for vibroacoustic problems. The specific structural formulations and mapping algorithms are discussed in the subsequent chapters.

3.1. Fluid–Structure Interaction

In FSI, the fluid occupies a time-dependent domain $\Omega_f(t)$ and interacts with a deformable structure occupying $\Omega_s(t)$. Their common boundary is denoted by $\Gamma_{fs}(t)$. For an incompressible Newtonian fluid, conservation of momentum and mass in an arbitrary Lagrangian–Eulerian (ALE) description can be written as

$$\rho_f\left(\frac{\partial v_f}{\partial t}\Big|_{\chi} + \left(v_f - v_m\right)\cdot \nabla v_f\right) - \nabla\cdot\sigma_f = \rho_f b_f,$$

$$\nabla\cdot v_f = 0,$$

where ρ_f is the fluid density, v_f the fluid velocity, v_m the mesh velocity, b_f the body force per unit mass, and χ the ALE coordinate. The Cauchy stress tensor is given by

$$\sigma_f = -pI + 2\mu\varepsilon\left(v_f\right), \qquad \varepsilon\left(v_f\right) = \frac{1}{2}\left(\nabla v_f + \nabla v_f^T\right).$$

The structural problem is governed by momentum balance together with the constitutive relations and kinematic assumptions of the selected structural model. In a reference configuration, the balance equation can be expressed as

$$\rho_{s,0}\ddot{d}_s = \nabla_0\cdot P + \rho_{s,0} b_s,$$

where d_s is the structural displacement, $\rho_{s,0}$ the reference density, and P the first Piola–Kirchhoff stress tensor. In the applications discussed later, the structural discretization may be based on an IBRA shell formulation or an isogeometric beam model. The latter requires a separate reconstruction of the wetted interface from its reduced-dimensional kinematics.

At the fluid–structure interface, the kinematic condition requires compatibility between fluid motion and structural motion. The dynamic condition requires equilibrium of the interface tractions:

$$v_f = \dot{d}_s, \qquad \sigma_f n_f + \sigma_s n_s = 0 \quad on\ \Gamma_{fs}(t).$$

Here the traction balance is expressed using outward normals of the corresponding current domains. In practice, the fluid and structural interface discretizations may not coincide, and the kinematic and dynamic quantities must be transferred between their respective approximation spaces.

3.2. Interface Data Transfer

For compatible discrete interface vectors, a linear displacement transfer can be expressed as

$$d_f = H_{fs} d_s,$$

where H_{fs} maps the structural interface degrees of freedom to the fluid-side representation. If f_f denotes the assembled discrete fluid interface force vector, the work-conjugate structural force vector is obtained through

$$f_s = H_{fs}^T f_f.$$

Consequently, for compatible virtual variations,

$$\delta d_s^T f_s = \delta d_f^T f_f.$$

These expressions describe a general algebraic requirement rather than a particular mapping algorithm. A distinction must be maintained between transferring assembled forces and transferring distributed tractions, which additionally requires an appropriate interface integration procedure. For geometrically nonlinear beam coupling, the kinematic transfer is configuration-dependent and its consistent linearization is needed to relate interface forces to generalized beam forces and moments. The detailed construction of those operators is addressed separately.

3.3. Partitioned Solution Procedure

In a partitioned Dirichlet–Neumann scheme, an estimate of the structural interface motion is prescribed to the fluid solver. The resulting fluid loads are transferred to the structural solver, which computes an updated interface displacement. In a strongly coupled procedure, this sequence is repeated until the interface residual satisfies a prescribed convergence criterion. A generic interface fixed-point problem can be written as

$$d_\Gamma = S\left(F\left(d_\Gamma\right)\right),$$

where F and S denote the fluid and structural solution operations, including the required interface transfer. The fixed-point residual is

$$r_\Gamma^{(k)} = S\left(F\left(d_\Gamma^{(k)}\right)\right) - d_\Gamma^{(k)}.$$

The convergence behavior depends on the coupled physics, the time discretization, the interface transfer, and the selected coupling algorithm. Relaxation and interface quasi-Newton methods may be used to accelerate the iterations. Their purpose is distinct from that of spatial mapping: acceleration updates the coupled interface solution, whereas mapping represents exchanged fields on different discretizations.

3.4. Frequency-Domain Vibroacoustic Coupling

The vibroacoustic application considers time-harmonic structural vibration and acoustic pressure. With a complex-amplitude convention proportional to $e^{i\omega t}$, a linear structural frequency-domain model may be written as

$$\left(K + i\omega C - \omega^2 M\right)\hat{u} = \hat{f}_{ext} + \hat{f}_{ac},$$

where K, C, and M are the stiffness, damping, and mass matrices, and $\hat{f}_{ac}$ denotes acoustic loading. For a homogeneous acoustic fluid, the complex pressure amplitude satisfies the Helmholtz equation

$$\nabla^2 \hat{p} + k^2 \hat{p} = 0, \qquad k = \frac{\omega}{c},$$

where c is the sound speed. At the structural–acoustic interface, the normal fluid velocity is compatible with the structural normal velocity, while acoustic pressure contributes to the surface traction. For the stated harmonic convention, the normal velocity condition can be expressed as

$$\hat{v}_f \cdot n = i\omega \hat{u} \cdot n.$$

The corresponding pressure–traction sign depends on the chosen normal orientation. In the investigated partitioned framework, the structural and acoustic solvers retain their own discretizations and exchange the required complex-valued interface quantities. Strong two-way coupling leads to a frequency-dependent interface fixed-point problem, for which complex-valued convergence acceleration can be employed. The acoustic boundary-element formulation and the numerical coupling strategies are presented in the vibroacoustic chapter.

4. Interface Mapping

The coupling of Isogeometric B-Rep Analysis (IBRA) with conventional finite-element or finite-volume discretizations requires the exchange of interface quantities between independently defined approximation spaces. Unlike a matching-mesh coupling, the two interfaces may differ in their element topology, spatial resolution, and locations at which the discrete fields are available. The problem is particularly relevant for IBRA because the physical interface is described by spline surfaces, while the control points generally do not coincide with points on the surface.

The mapping study considered here compares established transfer approaches in the context of CAD-integrated fluid–structure interaction (FSI). Its scope extends beyond interpolation error to include the conservation properties of load transfer, the influence of trimming and multipatch representations, computational cost, and the effect of mapping on a partitioned coupled solution. The discussion below summarizes the principles and assessment criteria; the full algorithmic developments and numerical datasets remain in the unpublished source manuscript.

4.1. Interface Representation and Transfer Requirements

Consider two discrete representations of a common physical coupling interface, denoted by Γ_o and Γ_d for the origin and destination, respectively. An origin field u_o must be reconstructed at the locations required by the destination discretization. For a linear transfer, the operation may be represented in discrete form as

$$u_d = H_{do} u_o,$$

where H_{do} denotes the mapping operator. Its construction depends on the origin and destination representations and on the physical quantity being transferred.

For a spline-based origin interface, a field is evaluated from its basis functions and control variables:

$$u_o^h(\xi, \eta) = \sum_{A=1}^{n_o} R_A(\xi, \eta) u_{o,A}.$$

Thus, a destination point on the physical surface may require a geometric projection into the origin patch's parametric domain before the field can be evaluated. For trimmed or multipatch interfaces, the projection and integration procedures must additionally respect active patch regions and internal patch boundaries.

Kinematic transfer should accurately reproduce the displacement or velocity field needed to impose interface compatibility. Dynamic transfer has an additional requirement: the mapped loading must be interpreted consistently with the discrete interface forces and their associated virtual work. If a displacement operator maps structural degrees of freedom to the fluid interface, the transpose operator provides a work-conjugate transfer of assembled discrete forces:

$$d_f = H_{fs} d_s, \qquad f_s = H_{fs}^T f_f.$$

The corresponding discrete work identity is

$$\delta d_s^T f_s = \delta d_f^T f_f.$$

This algebraic property must not be confused with direct interpolation of a traction field. In the latter case, the mapped traction must be integrated against the destination shape functions to obtain structural forces.

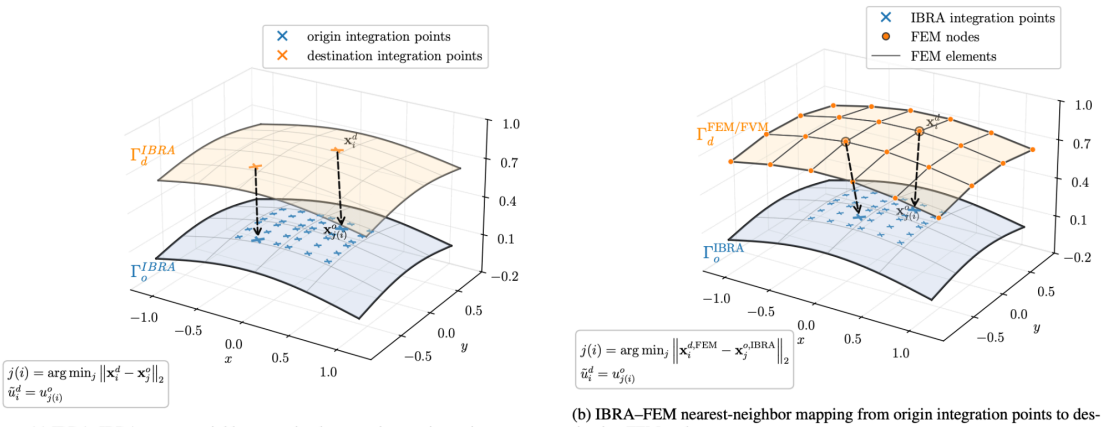
4.2. Mapping Strategies

4.2.1. Nearest-Neighbor Mapping

Nearest-neighbor mapping assigns to each destination location the value associated with its closest origin sampling point. The closest-point relation can be written as

$$j(i) = arg\,min_j \|x_{d,i} - x_{o,j}\|_2, \qquad \tilde{u}_{d,i} = u_{o,j(i)}.$$

The method is straightforward to construct and inexpensive to apply. However, it does not reconstruct the variation of the origin field within an element or spline patch. Consequently, its accuracy may be limited for coarse or strongly non-matching interfaces, especially when the transferred field varies significantly in space. The source study considers nearest-neighbor mapping both between IBRA integration points and between IBRA integration points and conventional FEM nodes.



(a) IBRA–IBRA nearest-neighbor mapping between integration points.

(b) IBRA–FEM nearest-neighbor mapping from origin integration points to destination FEM nodes.

Figure 4: *Nearest-neighbor mapping between non-matching origin and destination interfaces for the IBRA–IBRA and IBRA–FEM cases.*

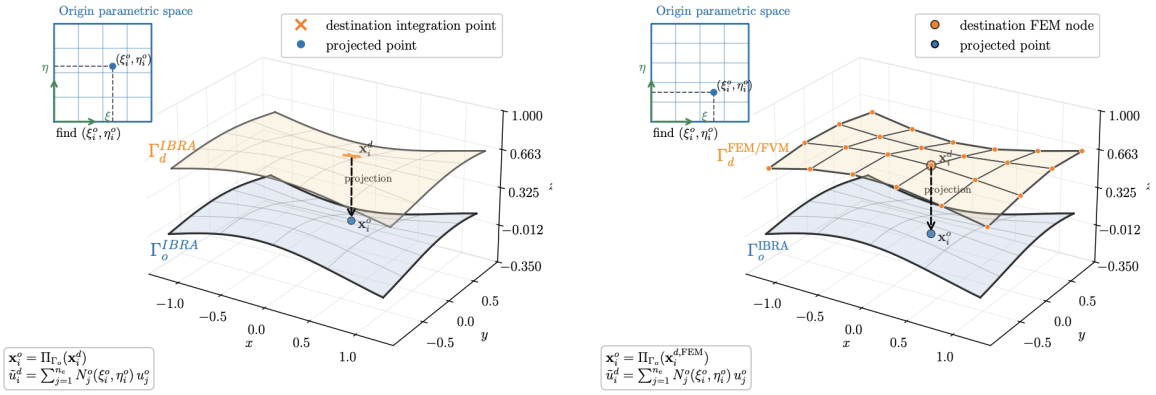
4.2.2. Nearest-Element Mapping

Nearest-element mapping accounts for the geometry and interpolation of the origin discretization. For each destination point, a closest projection is identified on an origin element or spline patch. The transferred value is then evaluated using the origin approximation at the projected location:

$$\tilde{u}_{d,i} = \sum_{A=1}^{n_e} N_A\left(\xi_{o,i}\right) u_{o,A},$$

where $\xi_{o,i}$ denotes the local coordinates of the projected point and N_A represents the corresponding origin basis. For an IBRA origin interface, this operation involves the underlying spline geometry and basis functions. Compared with nearest-neighbor transfer, the method

uses more information about the source field, although its reliability still depends on the geometric projection and the treatment of patch boundaries.



(a) IBRA–IBRA nearest-element mapping.

(b) IBRA–FEM nearest-element mapping.

Figure 5: *Nearest-element mapping between non-matching origin and destination interfaces for the IBRA–IBRA and IBRA–FEM cases.*

4.2.3. Radial Basis Function Mapping

Radial basis function (RBF) mapping constructs an interpolant from scattered origin samples. A scalar component of the transferred field can be expressed generically as

$$s(x) = \sum_{j=1}^{n_o} \alpha_j \phi\left(\| x - x_{o,j} \|\right) + p(x),$$

where ϕ is a radial kernel, α_j are interpolation coefficients, and p is an optional polynomial contribution. The coefficients are determined from interpolation conditions at the origin points, with additional constraints where required by the chosen formulation.

The source investigation considers thin-plate spline and compactly supported Wendland kernels. These alternatives offer different interpolation and sparsity characteristics. Their practical behavior depends on the spatial distribution of sampling points, kernel selection, support parameters, and the conditioning and cost of constructing the interpolant.

4.2.4. Mortar Mapping

Mortar mapping establishes a relation between the origin and destination fields through a weak projection over their common interface. For a scalar field, the standard L^2 projection seeks a destination approximation satisfying

$$\int_\Gamma N_{d,A}\left(u_d^h - u_o^h\right) d\Gamma = 0 \quad for\ each\ destination\ test\ function\ N_{d,A}.$$

This gives a matrix system of the form

$$M_{DD} u_d = M_{DO} u_o,$$

where the matrices contain integrals of products of destination and origin basis functions. Their evaluation requires integration over the overlapping physical interface, despite the independent parameterizations and discretizations.

For IBRA–FEM coupling, the construction of the common integration domain requires particular attention due to the different geometric representations of the participating interfaces. As illustrated in Figure 6, the procedure begins by projecting the FEM interface elements onto the exact IBRA surface and subsequently into the parametric space of the corresponding NURBS patches. The projected regions are then subdivided along the knot lines and triangulated to define the integration subdomains over which numerical quadrature is performed. In multipatch configurations, FEM elements may overlap several patches, requiring the integration domain to be constructed separately for each affected patch.

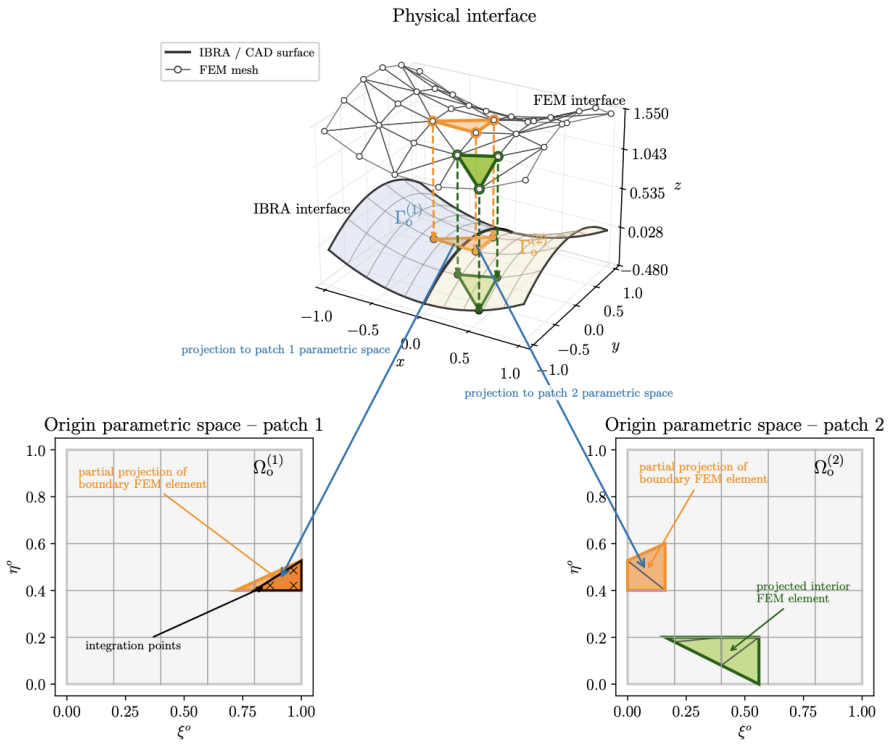
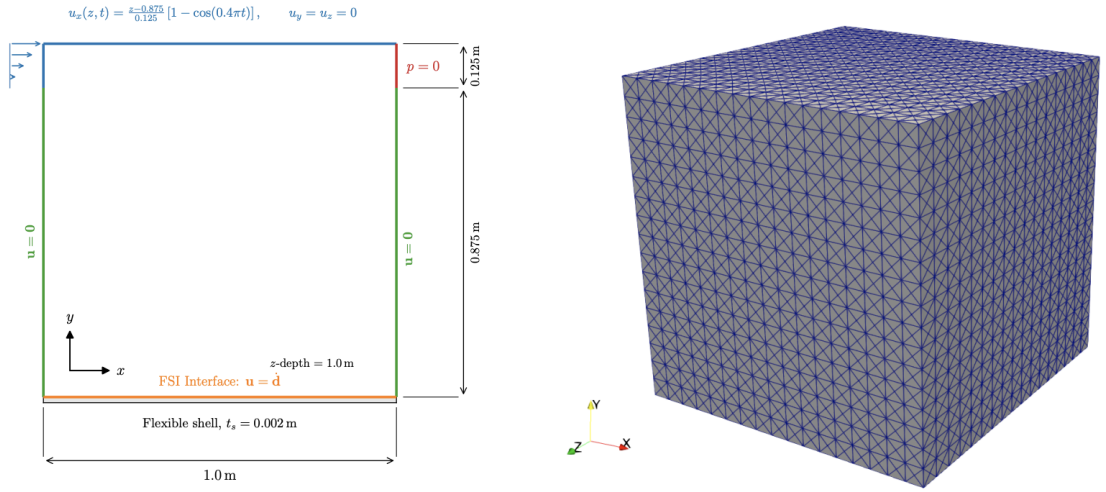


Figure 6: *Construction of the common integration domain for the IBRA–FEM mortar mapper*

4.3. Numerical Assessment: Three-Dimensional Lid-Driven Cavity

The numerical assessment is restricted to the three-dimensional lid-driven cavity benchmark with a flexible structural interface. This configuration is used to compare the investigated mapping strategies in terms of coupled structural response, coupling convergence, spatial mapping accuracy, and computational cost. The same fluid and structural discretizations, time integration settings, and coupling parameters are retained across the mapping comparisons, so that differences can be attributed primarily to the transfer procedure. The structural interface is represented by an isogeometric Kirchhoff–Love shell, while the fluid uses a conventional discretization.

The coupled calculation employs a strongly coupled partitioned Gauss–Seidel procedure with IQN-ILS acceleration applied to the transferred structural loads. The time-step size is $\Delta t = 0.025\,s$, and the relative coupling load-residual tolerance is 10^{-6}. These settings are common to the investigated mapping strategies.



(a) x–z cross-section and fluid boundary conditions.

(b) Three-dimensional fluid discretization.

Figure 7: *Three-dimensional lid-driven cavity benchmark, (a) boundary conditions, (b) Fluid discretization*

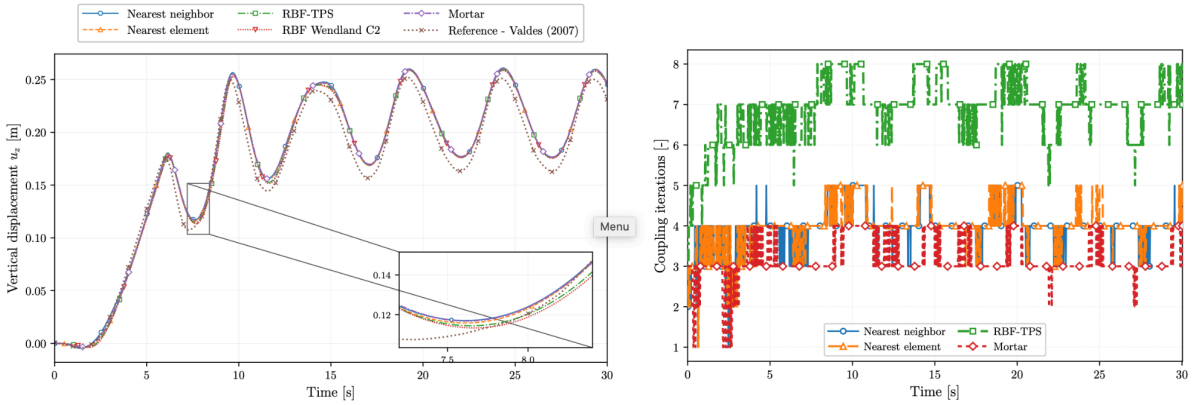
Parameter	Symbol	Value
Fluid density	ρ_f	$1.0\,\mathrm{kg/m^3}$
Dynamic viscosity	μ_f	0.01 Pa s
Structural density	ρ_s	$500\,\mathrm{kg/m^3}$
Young's modulus	E	250 Pa
Poisson's ratio	ν	0
Shell thickness	t_s	2×10^{-3} m

Table 1: *Material and geometric parameters of the lid-driven cavity benchmark*

4.3.1. Midpoint Displacement and Coupling Iterations

The influence of interface mapping on the coupled response is first assessed from the vertical displacement of the flexible shell at its midpoint, located at $(x, y, z) = (0.5, 0.5, 0)\,m$. The displacement histories obtained with nearest-neighbor, nearest-element, mortar, and RBF mapping are compared with the reference solution of Valdes (2007). Figure 8(a) of the source manuscript shows that the investigated strategies predict closely comparable displacement histories and reproduce the reference response reasonably well.

The number of coupling iterations required to satisfy the prescribed convergence criterion is shown in Figure 8(b). Despite the similarity of the structural responses, the mapping methods differ in their influence on iterative convergence. Nearest-neighbor, nearest-element, and mortar mapping generally require comparable iteration counts, while RBF-TPS requires more iterations. Mortar mapping achieves the lowest average number of coupling iterations among the tested approaches. These observations underline that agreement in the primary response quantity does not necessarily imply identical coupling performance.



(a) Midpoint vertical displacement for the different interface mappers using conservative load mapping, compared with the reference results of Valdes (2007).

(b) Coupling iterations per time step.

Figure 8: *Influence of the interface mapping strategy on the three-dimensional lid-driven cavity problem: (a) vertical displacement magnitude at the midpoint of the flexible shell; (b) number of coupling iterations required for convergence at each time step.*

4.3.2. Spatial Convergence of the Mapping Error

The spatial accuracy of the mapping operators is assessed by fixing the IGA origin discretization and successively refining the FEM destination interface. The mapped displacement is compared with a reference field obtained by evaluating the IGA solution directly at the destination interface. The relative L^2 error is defined as

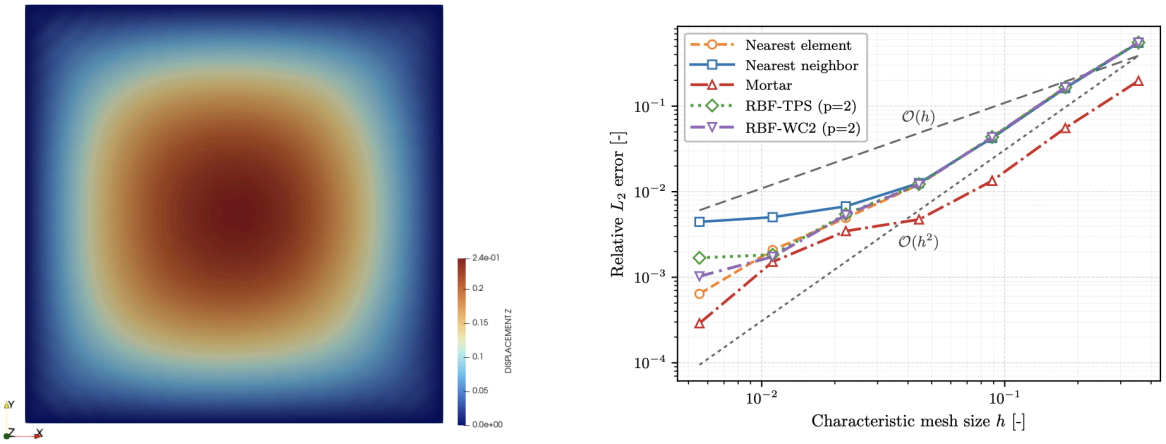
$$e_{L^2} = \left(\frac{\int_{\Gamma_{fs}} \| u_h^{map} - u^{ref} \|^2 \, d\Gamma}{\int_{\Gamma_{fs}} \| u^{ref} \|^2 \, d\Gamma} \right)^{1/2} .$$

Two displacement fields from the same FSI simulation are considered to investigate the influence of the spatial characteristics of the transferred field on mapping accuracy.

At $t = 10s$, the displacement field is relatively smooth and dominated by low-frequency spatial variations, as illustrated in Figure 9(a). The corresponding convergence results, presented in Figure 9(b), show approximately first-order convergence for nearest-neighbor mapping, whereas nearest-element, mortar, and RBF-TPS mapping achieve approximately second-order convergence.

At $t = 2s$, the displacement field exhibits stronger spatial variations, as shown in Figure 10(a). In this case, the convergence results in Figure 10(b) indicate that all investigated mapping strategies approach approximately first-order convergence.

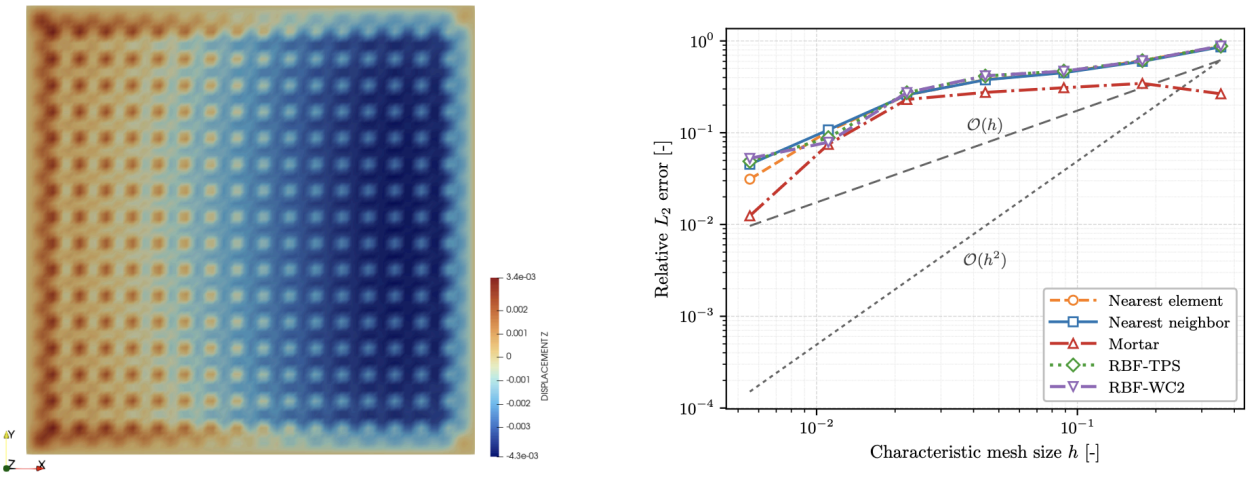
These results demonstrate that the observed convergence order depends not only on the mapping algorithm but also on the spatial characteristics of the transferred field. In particular, higher-order convergence observed for smooth displacement distributions may deteriorate when the field contains stronger spatial variations.



(a) Reference IGA displacement field.

(b) Relative L^2 displacement error.

Figure 9: *Spatial convergence study for the smooth displacement field at $t = 10s$: (a) reference displacement field and (b) relative L^2 mapping error under mesh refinement.*



(a) Reference IGA displacement field.

(b) Relative L^2 displacement error.

Figure 10: *Spatial convergence study for the displacement field at $t = 2s$: (a) reference displacement field and (b) relative L^2 mapping error under mesh refinement.*

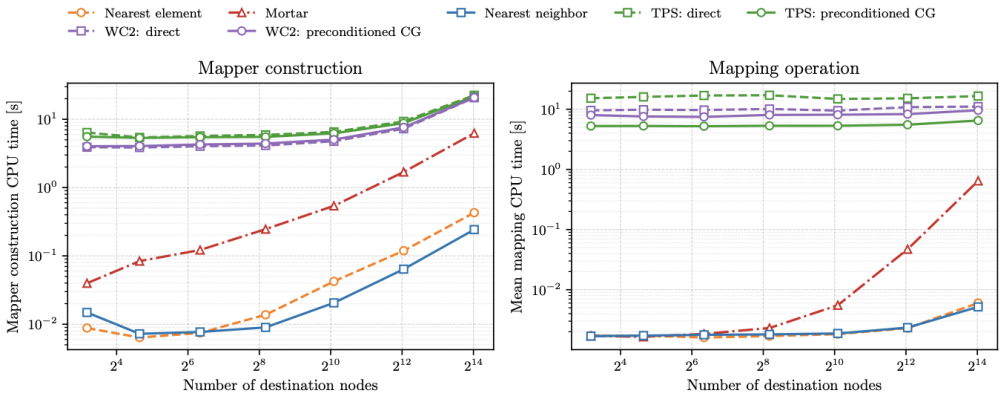
4.3.3. Computational Cost

Computational performance is evaluated by separating the CPU time required to construct the mapping operator from the time required for its subsequent application. Two complementary refinement studies are considered, as presented in Figure 11. In the first study, the IGA origin discretization is held fixed while the FEM destination interface is progressively refined (Figure 11(a)). In the second, the FEM destination discretization remains fixed while the number of IGA origin control points is increased (Figure 11(b)). All measurements are performed using identical hardware and parallelization settings.

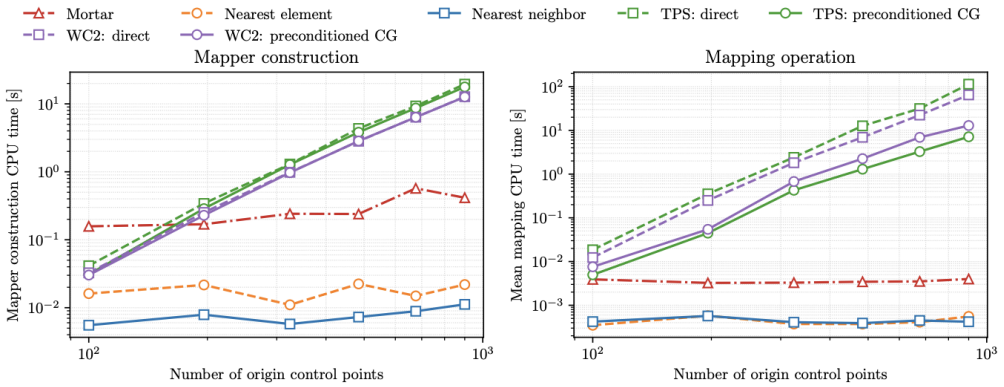
The results in Figure 11 show that nearest-neighbor and nearest-element mapping exhibit the lowest construction and application costs among the investigated strategies. Mortar mapping

requires a more expensive operator construction, while its application cost increases with destination refinement and remains less sensitive to origin refinement. In contrast, RBF-based methods are more sensitive to the number of origin control points, with both construction and application times increasing as the origin discretization is refined.

The comparison also highlights the influence of the linear solution strategy on the computational performance of RBF mapping. For larger origin discretizations, the compactly supported Wendland formulation is less expensive than thin-plate spline interpolation when a direct solver is employed. However, using a preconditioned conjugate-gradient solver substantially reduces the computational cost of both RBF approaches, particularly for thin-plate splines. These results indicate that computational efficiency depends not only on the mapping formulation but also on its numerical implementation.



(a) Fixed IGA origin discretization with successively refined FEM destination discretizations.



(b) Fixed FEM destination discretization with successively refined IGA origin discretizations.

Figure 11: *Spatial convergence study for the displacement field at $t = 2s$: (a) reference displacement field and (b) relative L^2 mapping error under mesh refinement.*

4.4. Discussion

The lid-driven cavity benchmark provides a consistent comparison of interface mapping methods at three complementary levels: the coupled structural response, the spatial transfer error, and the computational effort. The midpoint displacement histories are similar for the investigated approaches, but the coupling iteration counts reveal differences that are not apparent from the response curves alone. The convergence studies further show that mapping

accuracy depends on the spatial characteristics of the transferred field, while the timing measurements demonstrate that operator construction and application can respond differently to origin and destination refinement.

These findings do not establish a universally preferable mapper. Rather, they show why interface transfer should be evaluated according to the accuracy required by the coupled application, the available interface resolution, and the expected frequency of operator construction and application. The next section considers a distinct transfer problem in which the fluid interface must be reconstructed from a geometrically nonlinear isogeometric beam rather than mapped directly between two surface discretizations.

5. Consistent Beam Mapping for Fluid-structure Interaction

The mapping strategies discussed in the preceding section transfer quantities between independently discretized interfaces. A different interface problem arises when a slender structure is represented by a one-dimensional beam, while the fluid solver resolves its finite-thickness boundary. The beam centerline does not directly describe the wetted interface. Consequently, the displacement of each fluid-interface point must be reconstructed from the beam translation and cross-sectional rotation, and the distributed fluid loading must be transferred back to the generalized beam degrees of freedom.

The present framework considers geometrically nonlinear isogeometric Bernoulli and Timoshenko beams. Both formulations describe the centerline using spline basis functions, but differ in their treatment of cross-sectional orientation. The mapping therefore follows the kinematics of each structural model rather than relying on a purely distance-based interpolation. The numerical assessment in this report is restricted to the Mok FSI benchmark.

5.1. Beam Kinematics and Interface Reconstruction

The reference centerline of an isogeometric beam can be expressed as

$$X_c(\xi) = \sum_{A=1}^{n} N_A(\xi) P_A,$$

where N_A are the spline basis functions and P_A the control points. The current centerline follows from the interpolated displacement field,

$$x_c(\xi) = X_c(\xi) + u_c(\xi).$$

A point Q on the fluid–structure interface is associated with the beam in the reference configuration. Its attachment is defined by a fixed centerline parameter ξ_Q and cross-sectional coordinates $\rho_{2,Q}$ and $\rho_{3,Q}$. Using reference material directors A_2 and A_3, its reference position is

$$X_Q = X_c(\xi_Q) + \rho_{2,Q} A_2(\xi_Q) + \rho_{3,Q} A_3(\xi_Q).$$

The reference attachment procedure is illustrated in Figure 12. Each fluid-interface point is projected onto the continuous reference beam centerline to identify its longitudinal parameter and associated cross-section. The offset from the projected centerline point is then resolved along the two reference cross-sectional directors. These attachment coordinates are computed in the reference configuration and remain fixed during subsequent deformation. This distinction between a fixed material attachment and a configuration-dependent interface reconstruction is central to the mapping approach.

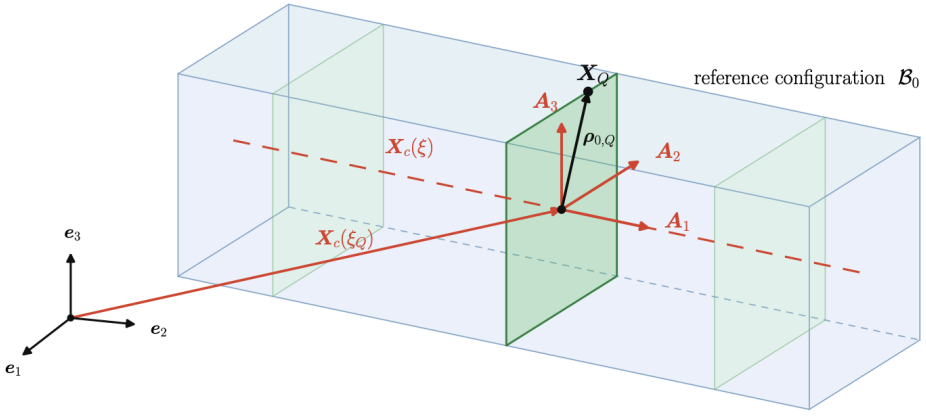


Figure 12: *Reference attachment of a fluid-interface point to the isogeometric beam. The closest-point projection identifies the centerline parameter and associated cross-section, while the reference offset is expressed using the cross-sectional material directors.*

During deformation, the same attachment coordinates are retained. The current interface position is reconstructed from the current centerline and material directors:

$$x_Q = x_c(\xi_Q) + \rho_{2,Q} a_2(\xi_Q) + \rho_{3,Q} a_3(\xi_Q), \qquad u_Q = x_Q - X_Q.$$

For the Bernoulli beam, the cross-section remains perpendicular to the current centerline tangent, with an additional twist about that tangent. For the Timoshenko beam, the cross-section has an independent rotational field and may undergo transverse shear deformation. The same geometric attachment procedure can therefore be used for both formulations, while the reconstruction of the current directors differs according to the beam theory.

This distinction is important for geometrically nonlinear motion: rotation of a cross-section displaces surface points even when the corresponding centerline point undergoes little translation. It is also important that the attachment is defined on the continuous spline centerline, since isogeometric control points do not generally lie on the physical beam axis.

5.2. Consistent Transfer of Interface Loads

The reconstructed interface positions determine the kinematic information prescribed to the fluid solver. Conversely, fluid forces acting on the wetted interface must produce both generalized forces and moments in the beam. A force applied away from the centerline cannot be represented correctly by a transfer that retains only its translational contribution.

The mapping formulation relates virtual interface motion to admissible variations of the beam degrees of freedom. In discrete form, this relation may be written as

$$\delta u_f = H(q)\, \delta q,$$

where q collects the generalized beam unknowns and H depends on the current structural configuration. Requiring equality of discrete virtual work gives

$$\delta q^T f_b = \delta u_f^T f_f, \qquad f_b = H(q)^T f_f.$$

Here f_f denotes the assembled fluid-interface force vector and f_b the corresponding generalized beam loading. The use of the transpose of the kinematic variation operator establishes work conjugacy between the displacement and load transfers. The operator itself differs between the Bernoulli and Timoshenko formulations because their admissible rotational variations differ. The detailed linearizations are not reproduced in this report.

5.3. Numerical Assessment: Mok FSI Benchmark

5.3.1. Configuration and Coupling Interface

The Mok benchmark consists of a flexible wall attached to the lower boundary of a two-dimensional flow channel. The wall is clamped at its upstream end and undergoes large displacements as the incoming flow is gradually increased. The geometry and boundary conditions are illustrated in Figure 13. The flexible segment is $1.25\,m$ long and $0.005\,m$ thick. A prescribed parabolic inflow profile is ramped during the first $10\,s$, and the simulation continues to $25\,s$.

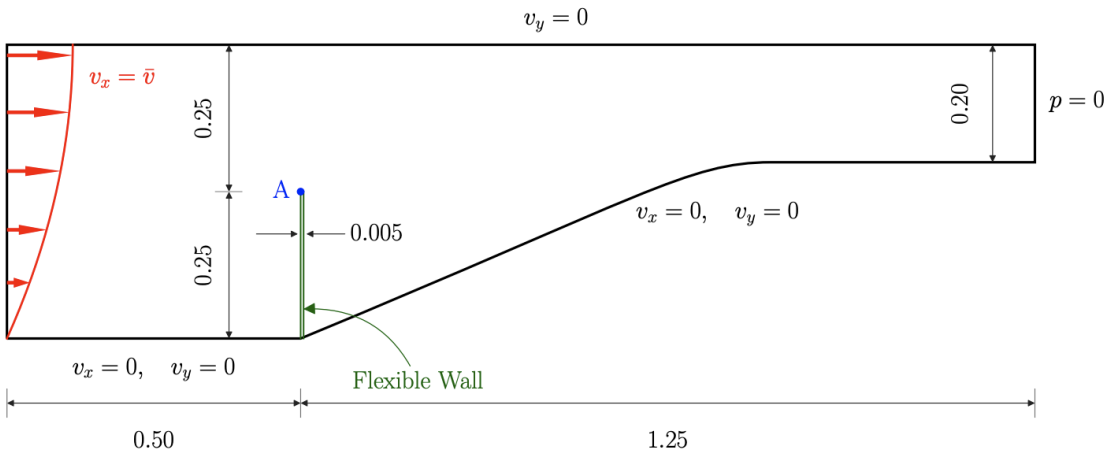


Figure 13: *Geometry and boundary conditions of the Mok fluid–structure interaction benchmark, adapted from Valdés.*

The fluid is modeled as an incompressible Newtonian fluid with density $\rho_f = 956\,kg/m^3$ and dynamic viscosity $\mu_f = 0.145\,Pa\,s$. The fluid mesh contains 6042 linear triangular elements. The flexible wall is modeled using geometrically nonlinear isogeometric Bernoulli and Timoshenko beams with Young's modulus $E = 2.3 \times 10^6\,Pa$, Poisson's ratio $\nu = 0.45$, and structural density $\rho_s = 1500\,kg/m^3$. Both beam models use a cubic B-spline centerline with eight knot spans and 11 control points.

The dimensional mismatch between the structural and fluid representations is illustrated in Figure 14. The fluid solver discretizes the finite-thickness wet boundary with linear interface elements, whereas the structural solver represents the wall through its one-dimensional centerline. At each coupling iteration, the beam motion is reconstructed at the fluid-interface points and the resulting fluid forces are mapped back to the beam's generalized degrees of freedom. The time step is $\Delta t = 0.025\,s$.

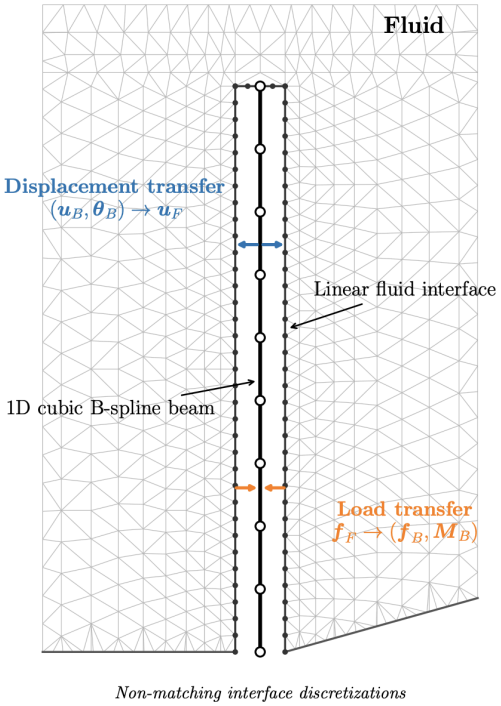


Figure 14: *Schematic representation of the non-matching coupling interface: transfer of beam displacement and rotation to the fluid boundary, and transfer of fluid forces to generalized beam forces and moments.*

5.3.2. Coupled Response

The deformation of the flexible wall and the surrounding fluid motion are illustrated in Figure 15 at $t = 8\,s$ and $t = 20\,s$. The snapshots show the evolution of the flow field and the substantial displacement of the wall during the transient simulation. They also provide a visual assessment of the reconstructed interface as it follows the nonlinear beam motion.

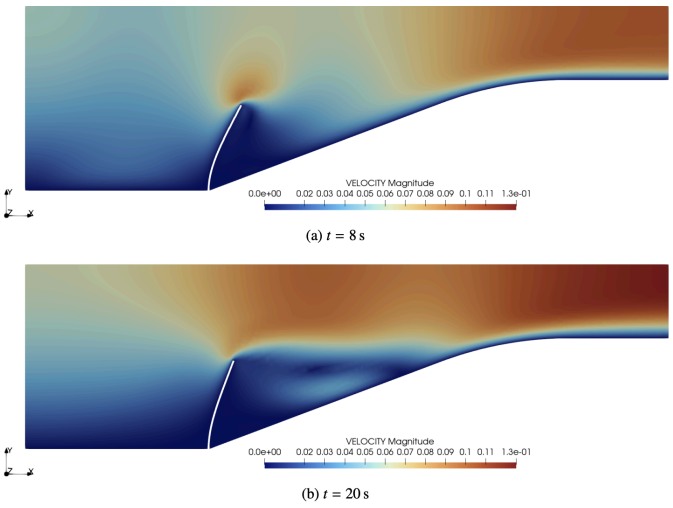
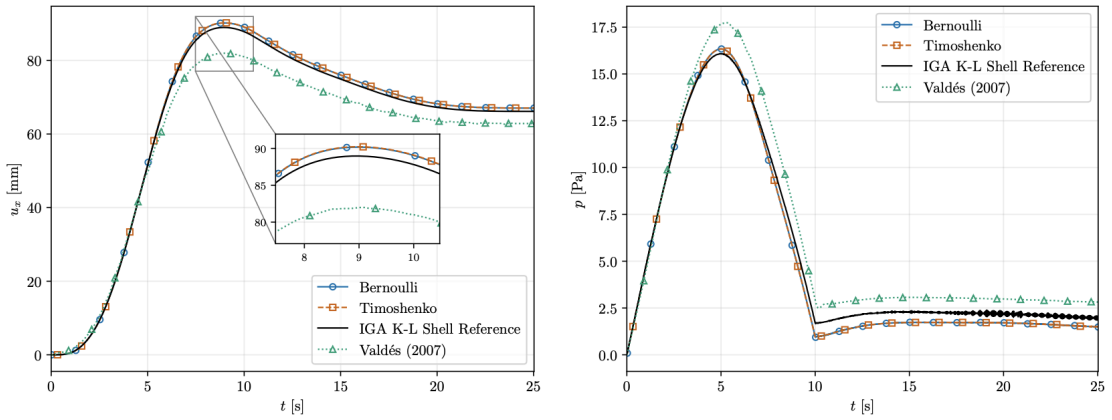


Figure 15: *Fluid velocity magnitude and deformed fluid–structure interface in the Mok benchmark at (a) $t = 8\,s$ and (b) $t = 20\,s$.*

The transient responses obtained with the Bernoulli and Timoshenko formulations are compared in Figure 16 with the published Valdés solution and an isogeometric Kirchhoff–Love shell reference computed using the same fluid mesh and coupling setup. The latter comparison isolates the influence of the reduced-dimensional structural representation and its interface mapping.

As shown in Figure 16(a), both beam models reproduce the evolution of the horizontal tip displacement and remain close to the shell reference. The maximum displacements are $90.18\,mm$ for Bernoulli and $90.22\,mm$ for Timoshenko, compared with $88.97\,mm$ for the shell model. The corresponding peak differences relative to the shell solution are 1.36% and 1.41%. Figure 16(b) shows the pressure history near the beam tip. Both beam formulations reproduce the characteristic early pressure maximum and subsequent decrease, with close agreement to the shell reference. The published Valdés response follows the same overall trends, although differences arise from the fluid and structural discretizations used in that study.



(a) Horizontal tip displacement.

(b) Pressure evolution at the beam tip.

Figure 16: *Transient response of the Mok benchmark for the Bernoulli and Timoshenko beam models, the isogeometric Kirchhoff–Love shell reference, and the Valdés reference: (a) horizontal tip displacement and (b) pressure evolution near the beam tip.*

5.4. Discussion

The Mok benchmark demonstrates the ability of the beam-to-surface mapping to couple one-dimensional isogeometric structural models with a fluid solver operating on a finite-thickness interface. The Bernoulli and Timoshenko formulations provide closely matching displacement and pressure histories and reproduce the principal features of the Kirchhoff–Love shell response. The discretization comparison further indicates that the coupled response can be represented using a compact beam centerline in this configuration.

The agreement is significant because the fluid-interface motion is not prescribed directly by the beam degrees of freedom: it must be reconstructed from centerline translations and cross-sectional orientations. Likewise, the fluid loading must be transferred into generalized beam forces and moments. The results therefore provide a coupled assessment of both transfer directions, while remaining specific to a problem in which rigid cross-sectional beam kinematics adequately represent the wall deformation.

6. Partitioned Co-simulation for CAD-integrated Vibroacoustic Analysis

The interaction between structural vibrations and acoustic wave propagation plays an important role in predicting sound radiation and fluid-induced structural response. For exterior acoustic problems, the boundary element method (BEM) is particularly suitable, as it allows unbounded fluid domains to be modeled without introducing artificial truncation boundaries. The framework presented in this section couples an isogeometric B-Rep analysis (IBRA) structural solver implemented in Kratos Multiphysics with an isogeometric BEM (IGA-BEM) acoustic solver developed in MATLAB. The two solvers operate independently, retaining their respective numerical formulations and spline-based geometric representations, while a partitioned co-simulation framework coordinates the exchange of interface quantities. A detailed description of the methodology and its numerical validation is provided in Camarotti and Le et al. [21].

6.1. Coupling Architecture and Interface Transfer

The framework operates in the frequency domain, where the displacement, velocity, pressure, and interface loads are complex-valued quantities. The structural harmonic problem is written as

$$\left(K - \omega^2 M + i\omega C\right)\hat{u} = \hat{F}_m + \hat{F}_a,$$

where the acoustic force $\hat{F}_a$ is obtained from the pressure field acting on the coupling interface. The structural interface motion supplies the normal-velocity boundary condition to the acoustic Helmholtz problem. The two solvers communicate through CoSimIO, and the independently discretized spline interfaces are connected using displacement and load transfer operators.

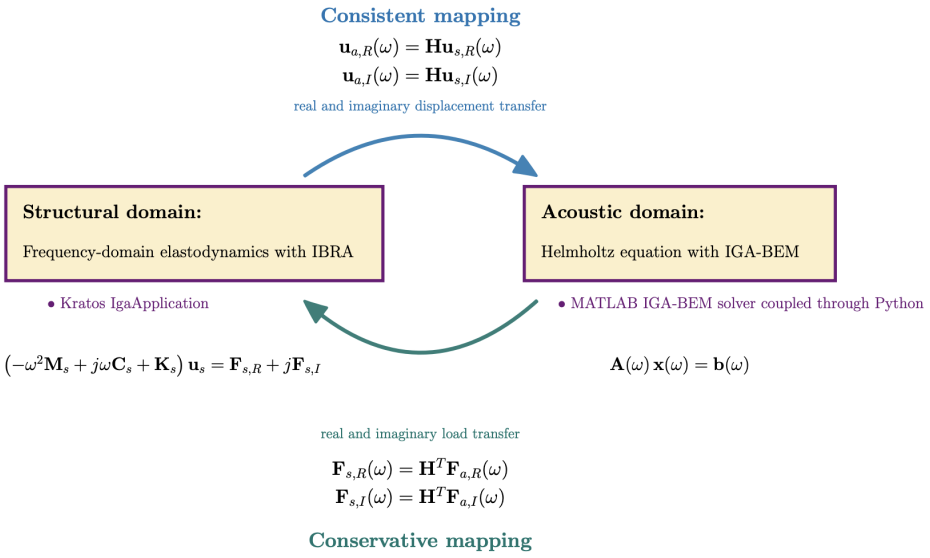


Figure 17: *Overview of the partitioned vibroacoustic co-simulation framework. The structural harmonic solver and acoustic Helmholtz solver exchange real and imaginary interface quantities through displacement and load transfer operators.*

As illustrated in Figure 17, the exchanged complex fields are communicated through their real and imaginary components. This data-exchange representation does not, however, require the two components to be treated independently in the coupling iterations. For a real-valued spatial transfer matrix H, the forward displacement mapping is applied to both components of the

complex displacement, and the transpose operator transfers acoustic loads back to the structural interface. This preserves the algebraic relation between forward and reverse transfer for the selected mapper.

6.2. Complex-Valued Convergence Acceleration

In a strongly coupled partitioned analysis, the structural and acoustic problems are solved repeatedly at each excitation frequency until the interface equilibrium residual satisfies the convergence criterion. Simple fixed-point iterations can converge slowly or diverge, especially near structural resonances. Frequency-domain coupling introduces an additional consideration: the interface residual is complex-valued, and its real and imaginary parts jointly describe the amplitude and phase of the response.

Let $x^{(k)}$ denote the current complex interface iterate and $\tilde{x}^{(k+1)}$ the value returned after one complete structural–acoustic coupling step. The fixed-point residual is

$$r^{(k)} = \tilde{x}^{(k+1)} - x^{(k)}.$$

The investigated complex-valued accelerators operate directly on this residual rather than accelerating the real and imaginary fields separately. Two variants of Aitken dynamic relaxation are considered: complex Aitken, which uses a Hermitian inner product to determine the relaxation factor, and complex modulus Aitken, which evaluates the update using the component-wise modulus of the complex residual. Both retain a scalar relaxation-based correction of the form

$$x^{(k+1)} = x^{(k)} + \alpha^{(k)} r^{(k)}.$$

The complex IQN-ILS method instead uses information from previous iterations to approximate the inverse interface Jacobian. Differences of complex residuals and returned interface values are collected in history matrices,

$$V = \left[\Delta r_1 \ \cdots \ \Delta r_m\right], \qquad W = \left[\Delta \tilde{x}_1 \ \cdots \ \Delta \tilde{x}_m\right].$$

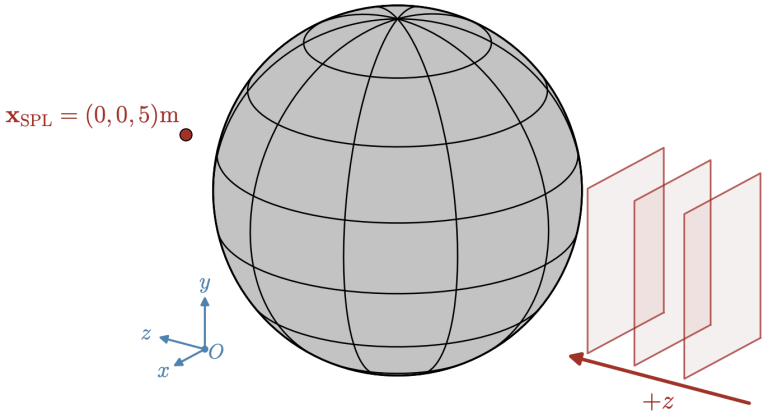
A complex least-squares problem, $Vc \approx - r^{(k)}$, provides coefficients for the interface update,

$$x^{(k+1)} = x^{(k)} + Wc + r^{(k)}.$$

Unlike a single relaxation parameter, the quasi-Newton correction can account for multiple directions of the coupled interface response. Working in the complex domain also retains the relation between amplitude and phase during the acceleration procedure. The proposed extensions are particularly relevant to strongly coupled vibroacoustic simulations, although their relative performance depends on the coupled problem.

6.3. Numerical Example: Spherical Shell in an Acoustic Fluid

The numerical assessment presented here is restricted to the spherical-shell benchmark. A thin spherical shell separates an enclosed acoustic fluid from an unbounded exterior acoustic domain and is excited by a harmonic plane wave propagating in the positive z-direction. The exterior pressure is evaluated at the observation point $x_{obs} = (0, 0, 5)\, m$. The configuration, shown in Figure 18, permits comparison with an analytical spherical-harmonic solution for the undamped case and with monolithic numerical references.



Property	Symbol	Value	Unit
Exterior fluid density	ρ_e	1000	kg/m^3
Exterior speed of sound	c_e	1500	m/s
Interior fluid density	ρ_i	1000	kg/m^3
Interior speed of sound	c_i	1500	m/s
Structural density	ρ_s	7850	kg/m^3
Young's modulus	E	210	GPa
Poisson's ratio	ν	0.30	–
Shell midsurface radius	a	3.5	m
Shell thickness	t	0.05	m
Incident pressure amplitude	A	1	Pa

Figure 18: *Spherical-shell benchmark with an enclosed acoustic domain, an unbounded exterior fluid, incident plane-wave excitation, and the exterior acoustic observation point.*

The structural and acoustic boundaries are represented independently, as illustrated in Figure 19. The structural shell consists of two trimmed NURBS patches and uses a Reissner–Mindlin formulation, with interpatch continuity imposed weakly. The acoustic boundary consists of six NURBS patches. Their distinct patch layouts and parameterizations create a non-conforming interface despite describing the same spherical geometry. Interface quantities are exchanged using nearest-element mapping, and strong coupling is accelerated using complex IQN-ILS.

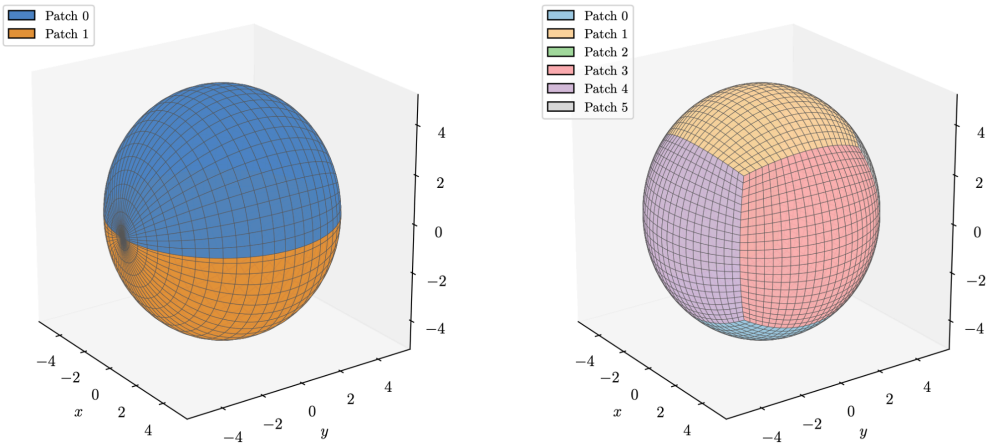


Figure 19: *Independent multipatch discretizations of the spherical-shell benchmark: two trimmed structural NURBS patches and six acoustic NURBS patches forming a non-conforming coupling interface.*

The frequency response is evaluated between 20 and 100 Hz for undamped and Rayleigh-damped structural configurations. Figure 20 compares the acoustic pressure magnitude predicted by the partitioned approach with the available analytical and monolithic reference solutions. The partitioned solution reproduces the principal resonance characteristics and pressure amplitudes. Differences become more pronounced near resonances, where the response is particularly sensitive to structural modeling, discretization, and interface transfer.

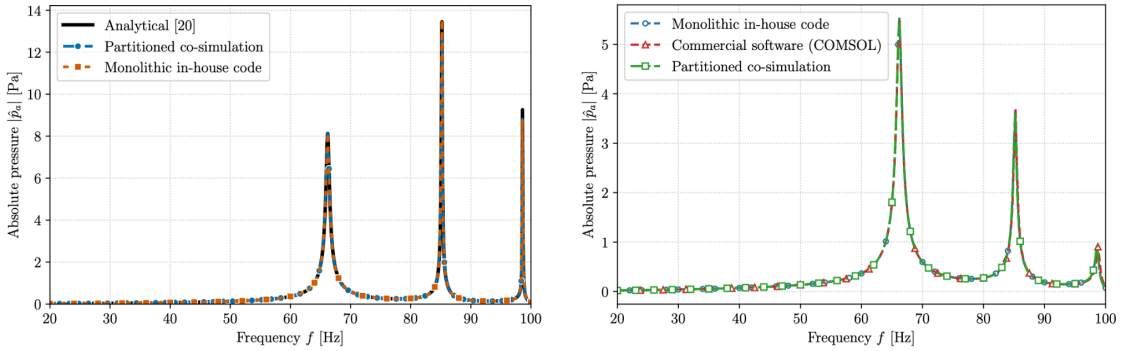


Figure 20: *Acoustic pressure magnitude at the exterior observation point for (a) undamped and (b) Rayleigh-damped spherical-shell configurations, compared with analytical and numerical reference solutions.*

Because frequency-domain pressure is complex-valued, agreement in magnitude alone is insufficient to characterize the coupled response. Figure 21 therefore compares the pressure phase angle for the damped configuration. The partitioned result closely follows the monolithic and commercial reference solutions, including the phase changes associated with resonance.

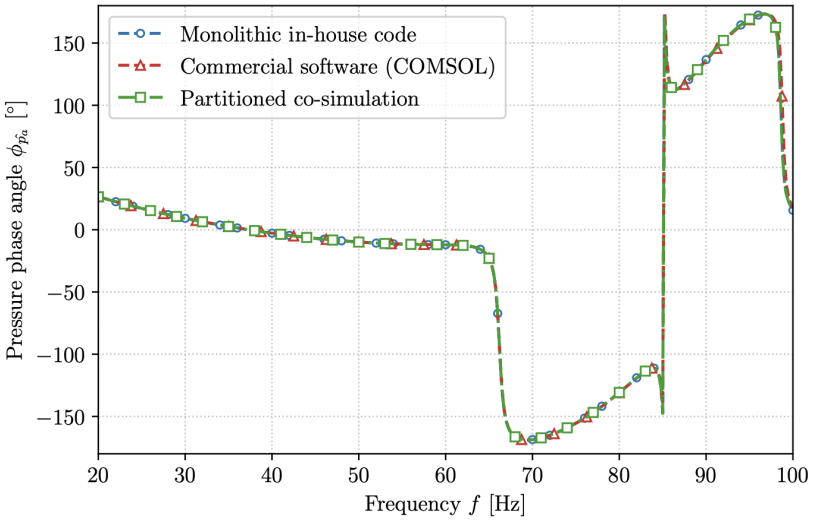
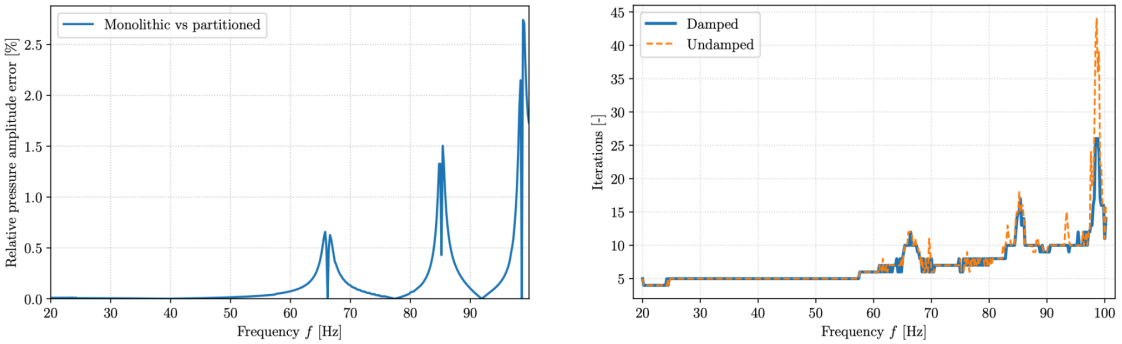


Figure 21: *Phase angle of the complex acoustic pressure at the observation point for the Rayleigh-damped spherical shell, compared with monolithic reference solutions.*

Figure 22 summarizes the relative pressure-amplitude error and the number of coupling iterations required by complex IQN-ILS. The amplitude error remains small over most of the

frequency range but increases around resonances. The iteration count similarly rises near resonance frequencies and at higher frequencies. Rayleigh damping moderates the pronounced iteration peaks by reducing the sensitivity of the structural response in these regions. These observations show that complex IQN-ILS can provide a converged partitioned solution for the investigated non-conforming spherical-shell problem, while the most demanding frequencies remain those close to structural resonances.



(a) Relative pressure amplitude error for the Rayleigh-damped case.

(b) Number of coupling iterations.

Figure 22: *Accuracy and convergence behavior of the spherical-shell partitioned solution using complex IQN-ILS: (a) relative acoustic pressure-amplitude error and (b) coupling iterations for undamped and Rayleigh-damped configurations.*

6.4. Discussion

The spherical-shell example demonstrates that the IBRA and IGA-BEM solvers can be coupled without imposing identical patch decompositions or discretizations on their shared interface. The results show agreement with reference solutions in both pressure magnitude and phase, and the convergence histories identify the increased difficulty of strong coupling near resonances. The complex-valued Aitken and IQN-ILS extensions address the need to accelerate frequency-domain interface iterations without artificially separating amplitude and phase. Within the spherical-shell benchmark, the numerical results specifically assess the complex IQN-ILS method; the relative performance of the alternative complex accelerators is not established by this example alone.

7. Conclusions

This report presented the development and assessment of partitioned co-simulation strategies for coupling isogeometric structural models with independently discretized fluid and acoustic domains. Particular attention was given to the interface treatment required when combining Isogeometric B-Rep Analysis (IBRA) with conventional finite element discretizations, reduced-dimensional beam models, and isogeometric boundary element formulations. The investigated approaches were designed to retain the flexibility of independently developed solvers while enabling consistent information exchange across non-matching interfaces.

The first part of the report addressed interface mapping between IBRA and FEM discretizations. Nearest-neighbor, nearest-element, radial basis function, and mortar-based mapping strategies were examined in terms of accuracy, convergence behavior, and computational cost. The three-dimensional lid-driven cavity benchmark demonstrated that the investigated algorithms can reproduce the coupled structural response, although their spatial convergence and computational requirements differ. In particular, the convergence studies highlighted the influence of the spatial characteristics of the transferred displacement field, while the computational assessment illustrated the trade-off between mapping accuracy and the cost of constructing and applying the transfer operators.

The report subsequently considered the coupling of geometrically nonlinear isogeometric Bernoulli and Timoshenko beams with fluid discretizations. A beam mapping framework was introduced in which fluid-interface points are attached to the reference beam centerline and subsequently reconstructed using the current centerline position and cross-sectional orientation. The corresponding load-transfer operators were obtained consistently from the linearization of the surface reconstruction, ensuring discrete virtual-work conjugacy. In the Mok FSI benchmark, both beam formulations closely reproduced the displacement and pressure responses of an isogeometric Kirchhoff–Love shell reference. These results demonstrated the suitability of the proposed mappings for representing fluid–structure interaction using reduced-dimensional structural models, provided that the underlying beam kinematics adequately describe the deformation.

Finally, a partitioned framework for frequency-domain vibroacoustic analysis was presented, coupling an IBRA structural solver with an isogeometric boundary element acoustic solver. The formulation enables the analysis of unbounded acoustic domains while retaining independent spline-based representations of the structural and acoustic interfaces. Particular emphasis was placed on the extension of Aitken dynamic relaxation and Interface Quasi-Newton with Inverse Least-Squares (IQN-ILS) acceleration to complex-valued interface quantities. By performing convergence acceleration directly in the complex domain, the proposed approach accounts for the amplitude and phase information inherent to harmonic response problems. The spherical-shell benchmark demonstrated good agreement with reference solutions in terms of acoustic pressure magnitude and phase, while confirming the effectiveness of complex IQN-ILS for strongly coupled frequency-domain simulations.

Overall, the investigations demonstrate that partitioned co-simulation provides a flexible framework for integrating isogeometric structural formulations into multiphysics analyses without requiring a monolithic implementation. At the same time, the results emphasize that the reliability and efficiency of such approaches depend on the treatment of the coupling interface, the consistency of displacement and load transfer, and the convergence behavior of the partitioned solution procedure. These aspects remain particularly important when extending the proposed methodologies to more complex CAD geometries, strongly coupled problems, and large-scale engineering applications.

8. REFERENCES

[1] Hughes, T. J. R., Cottrell, J. A., & Bazilevs, Y. (2005). Isogeometric analysis: CAD, finite elements, NURBS, exact geometry and mesh refinement. Computer Methods in Applied Mechanics and Engineering, 194(39–41), 4135–4195. https://doi.org/10.1016/j.cma.2004.10.008

[2] Bucher, P. (2023). CoSimulation and Mapping for Large Scale Problems. Doctoral dissertation, Technical University of Munich, Germany.

[3] Wang, T. (2016). Development of Co-Simulation Environment and Mapping Algorithms. Doctoral dissertation, Technical University of Munich, Germany.

[4] Wilson, P., Teschemacher, T., Bucher, P., & Wüchner, R. (2021). Non-conforming FEM-FEM coupling approaches and their application to dynamic structural analysis. Engineering Structures, 241, 112342. https://doi.org/10.1016/j.engstruct.2021.112342

[5] Apostolatos, A., Emiroğlu, A., Shayegan, S., Péan, F., Bletzinger, K.-U., & Wüchner, R. (2021). An isogeometric B-Rep mortar-based mapping method for non-matching grids in fluid–structure interaction. Advanced Modeling and Simulation in Engineering Sciences, 8, Article 9. https://doi.org/10.1186/s40323-021-00190-9

[6] Bauer, A. M. (2020). CAD-Integrated Isogeometric Analysis and Design of Lightweight Structures. Doctoral dissertation, Technical University of Munich, Germany.

[7] Dadvand, P., Rossi, R., & Oñate, E. (2010). An object-oriented environment for developing finite element codes for multi-disciplinary applications. Archives of Computational Methods in Engineering, 17, 253–297.

[8] Teschemacher, T., Bauer, A. M., Oberbichler, T., Breitenberger, M., Rossi, R., Wüchner, R., & Bletzinger, K.-U. (2018). Realization of CAD-integrated shell simulation based on isogeometric B-Rep analysis. Advanced Modeling and Simulation in Engineering Sciences, 5, Article 19. https://doi.org/10.1186/s40323-018-0109-4

[9] Mok, D. P. (2001). Partitionierte Lösungsansätze in der Strukturdynamik und der Fluid-Struktur-Interaktion. Doctoral dissertation.

[10] Turek, S., Hron, J., Razzaq, M., Wobker, H., & Schäfer, M. (2010). Numerical benchmarking of fluid–structure interaction: A comparison of different discretization and solution approaches. In Fluid Structure Interaction II: Modelling, Simulation, Optimization (pp. 413–424). Springer.

[11] Valdés Vázquez, J. G. (2007). Nonlinear Analysis of Orthotropic Membrane and Shell Structures Including Fluid–Structure Interaction. Doctoral dissertation, Universitat Politècnica de Catalunya, Spain.

[12] Irons, B. M., & Tuck, R. C. (1969). A version of the Aitken accelerator for computer iteration. International Journal for Numerical Methods in Engineering, 1(3), 275–277. https://doi.org/10.1002/nme.1620010306

[13] Degroote, J., Bathe, K.-J., & Vierendeels, J. (2009). Performance of a new partitioned procedure versus a monolithic procedure in fluid–structure interaction. Computers & Structures, 87(11–12), 793–801. https://doi.org/10.1016/j.compstruc.2008.11.013

[14] Degroote, J., Haelterman, R., Annerel, S., Swillens, A., Segers, P., & Vierendeels, J. (2008). An interface quasi-Newton algorithm for partitioned simulation of fluid–structure interaction. In Fluid–Structure Interaction: Theory, Numerics and Applications (pp. 55–64).

[15] Simpson, R. N., Scott, M. A., Taus, M., Thomas, D. C., & Lian, H. (2014). Acoustic isogeometric boundary element analysis. Computer Methods in Applied Mechanics and Engineering, 269, 265–290. https://doi.org/10.1016/j.cma.2013.10.026

[16] Lian, H., Simpson, R. N., & Bordas, S. P. A. (2013). Stress analysis without meshing: Isogeometric boundary-element method. Proceedings of the Institution of Civil Engineers – Engineering and Computational Mechanics, 166(2), 88–99. https://doi.org/10.1680/eacm.11.00024

[17] Junger, M. C., & Feit, D. (1986). Sound, Structures, and Their Interaction (2nd ed.). MIT Press.

[18] Cottrell, J. A., Hughes, T. J. R., & Bazilevs, Y. (2009). Isogeometric Analysis: Toward Integration of CAD and FEA. John Wiley & Sons.

[19] Bazilevs, Y., Calo, V. M., Hughes, T. J. R., & Zhang, Y. (2008). Isogeometric fluid–structure interaction: Theory, algorithms, and computations. Computational Mechanics, 43, 3–37. https://doi.org/10.1007/s00466-008-0315-x

[20] Benson, D. J., Bazilevs, Y., Hsu, M.-C., & Hughes, T. J. R. (2010). Isogeometric shell analysis: The Reissner–Mindlin shell. Computer Methods in Applied Mechanics and Engineering, 199, 276–289. https://doi.org/10.1016/j.cma.2009.05.011

[21] Camarotti, J. I., Le, P., Cai, Y., Aristio, R., Panagiotopoulos, D., Deckers, E., & Wüchner, R. (2026). Partitioned Co-Simulation for CAD-integrated Vibroacoustic Problems in Unbounded Domains. arXiv preprint, arXiv:2609.15384. https://doi.org/10.48550/arXiv.2609.15384

.